

The prismatic $\Sigma 3$ ($10\bar{1}0$) twin boundary in $\alpha\text{-Al}_2\text{O}_3$ investigated by density functional theory and transmission electron microscopy

Stefano Fabris, Stefan Nufer,* and Christian Elsässer

Max-Planck-Institut für Metallforschung, Seestrasse 92, D-70174 Stuttgart, Germany

(November 6, 2018)

The microscopic structure of the prismatic $\Sigma 3$ ($10\bar{1}0$) twin boundary in $\alpha\text{-Al}_2\text{O}_3$ is characterized theoretically by ab-initio local-density-functional theory, and experimentally by spatial-resolution electron energy-loss spectroscopy in a scanning transmission electron microscope (STEM), measuring energy-loss near-edge structures (ELNES) of the oxygen K -ionization edge. Theoretically, two distinct microscopic variants for this twin interface with low interface energies are derived and analysed. Experimentally, it is demonstrated that the spatial and energetical resolutions of present high-performance STEM instruments are insufficient to discriminate the subtle differences of the two proposed interface variants. It is predicted that for the currently developed next generation of analytical electron microscopes the prismatic twin interface will provide a promising benchmark case to demonstrate the achievement of ELNES with spatial resolution of individual atom columns.

I. INTRODUCTION

The local atomistic and electronic structures at extended defects in materials, such as grain boundaries in polycrystals or interfaces in layered nanostructures, are highly influential on the structural or functional properties of many technological devices, and hitherto, strong efforts have been made to characterize them microscopically. Recently, significant progress has been achieved by combining experimental imaging and spectroscopy with theoretical ab initio calculations. On the experimental side, imaging and electron-energy-loss spectroscopy (EELS) are combined via transmission electron microscopy (TEM) with sub-nm spatial and sub-eV energetical resolutions. On the theoretical side, the first-principles electronic structure calculations are based on the local density functional theory (LDFT). This current progress of TEM and LDFT has been demonstrated for instance for the rhombohedral $\Sigma 7$ ($\bar{1}012$) twin boundary in $\alpha\text{-Al}_2\text{O}_3$,^{1,2} a model case of a realistic interface in a technologically relevant ceramic material.

In the case of the rhombohedral twin boundary,¹ both the quantitative analysis of high-resolution TEM (HRTEM) and EELS were able to discriminate between the lowest-energy interface model and another metastable one, which were predicted by ab-initio LDFT calculations.² On the one side, for the high-resolution TEM combined with image simulation, the

*Present address: Robert Bosch GmbH, Robert-Bosch-Platz 1, D-70839 Gerlingen-Schillerhöhe, Germany.

discrimination was at the limits of the present experimental resolution and simulation accuracy. On the other side, the electron-energy-loss spectroscopy in a scanning transmission electron microscope (STEM) provided spatially resolved energy-loss near-edge structures (ELNES) in the oxygen K -ionization edge, which, in combination with calculated local densities of unoccupied one-electron states, yielded a more clear distinction between the lowest-energy and metastable higher-energy interface models.

In the present work, this effort in microscopic interface analysis is extended to the prismatic $\Sigma 3$ ($10\bar{1}0$) twin of α - Al_2O_3 . In this case, the theoretical LDFT analysis results again in two metastable low-energy interface models. In distinction from the rhombohedral-twin, it is demonstrated that experimental EELS in a STEM with spatial resolution of 1–2 nm, as in Ref. 1, is *not* sufficient to discriminate the ELNES of the theoretically predicted models for the prismatic twin interface. It is predicted that for a new generation of analytical TEM instruments with spatial resolution of 0.1–0.2 nm, which are currently under development in academic and industrial TEM research laboratories,³ the prismatic twin interface will provide a promising benchmark for a successful achievement of atom-column-resolution ELNES, via a site-specific comparison of measured oxygen K -ionization edges and calculated local densities of states. A further challenge for quantitative high-resolution TEM image analysis is provided by the calculated interfacial arrangement of atoms.

After a concise summary of the computational and experimental methods (Sec. II), we will report the search procedure for metastable variants of the twin boundary via empirical shell-model and ab-initio LDFT calculations (Sec. IIIA), the ab-initio LDFT analysis of the interfacial atomistics and energetics (Sec. IIIB), the calculated local densities of states and experimental ELNES (Sec. IIIC), and the simulated HRTEM images of the theoretically obtained two variants of the twin boundary (Sec. IIID). The main conclusions will be summarized in Sec. IV.

II. METHODS

A. Computational approaches

The theoretical analysis described in this work combines empirical atomistic modeling, based on an ionic shell-model potential,⁴ and first-principles electronic-structure calculations, based on the density-functional theory⁵ in the local-density approximation for exchange and correlation⁶ (local density functional theory, LDFT).

The shell-model potential was parameterized for α - Al_2O_3 by Lewis and Catlow⁷ via fitting to experimental and theoretical data. The potential describes the crystal as fully ionic, with long-range electrostatic interactions (point charges on both atomic sites and charged shells on the anion sites), short-range overlap repulsion, and weak van der Waals interactions. The model reproduces quite well the structural properties of bulk and defective α - Al_2O_3 , but fails to predict the energetic stability of the corundum structure relative to other possible polymorphs.^{8,9} In this work, the model is applied for a qualitative search of metastable translation states of α - Al_2O_3 (corundum) bicrystals, hence it is applied where its predictive power is well justified. The atomistic interface-structure variations with the shell-model potential are performed with the computer code GULP.¹⁰

In our first-principles mixed-basis pseudopotential LDFT approach,^{11–15} the crystal valence wave functions are represented by a mixed basis set, consisting of plane waves and localized functions. In the specific case of Al_2O_3 , the plane waves are limited by the maximum kinetic energy $E_{pw}=300$ eV. Three localized functions with angular momentum $l = 1$, $m = 0, \pm 1$, are centered at each oxygen site, and spatially confined by a sphere of radius $r_{lo}=1.16$ Å. The interactions of the atomic nuclei and core electrons on the valence electrons are described with norm-conserving non-local ionic pseudopotentials. More details on the construction of the pseudopotentials, and on the predictions of the method for the structural parameters of bulk $\alpha\text{-Al}_2\text{O}_3$ can be found in Ref. 2. The total energies for the prismatic twins are calculated by sampling the Brillouin zone of orthorhombic 120-atom supercells (see below) on a $2\times 1\times 1$ \mathbf{k} -point mesh. The forces on all atoms are explicitly calculated after self-consistency of the electronic structure is achieved, and thus the method allows for efficient structural relaxation of the atomic positions.

The crystal structure of $\alpha\text{-Al}_2\text{O}_3$ (corundum or sapphire, space group $R\bar{3}c$), projected on the $(\bar{1}2\bar{1}0)$ plane, is shown in Fig. 1: light and dark circles represent oxygen and aluminium ions, respectively, and the dashed line marks a prismatic $(10\bar{1}0)$ plane. The twin boundaries are modeled with 120-atom orthorhombic supercells. These are defined by the lattice vectors $\mathbf{e}_1=[\bar{1}2\bar{1}0]$, $\mathbf{e}_2=[0001]$, and $\mathbf{e}_3=[10\bar{1}0]$. The supercell contains two grains of $\alpha\text{-Al}_2\text{O}_3$ with a misorientation given by $(10\bar{1}0)\parallel(10\bar{1}0)$ and $[1\bar{2}10]\parallel[\bar{1}2\bar{1}0]$: the three-dimensional periodic repetition generates a sequence of equivalent interfaces, separated by 6.8 Å thick slabs of bulk corundum.

B. Experimental procedures

The prismatic twin bicrystal of $\alpha\text{-Al}_2\text{O}_3$ was prepared by W. Kurtz, MPI für Metallforschung Stuttgart, by diffusion bonding¹⁶ of two halves of highly pure single crystals of sapphire in ultra-high vacuum. The resulting bicrystal has a deviation of $\approx 0.1^\circ$ from the perfect misorientation (measured by electron and X-ray diffraction). The impurity concentration at the interface was below the detection limit of energy-dispersive X-ray (EDX) spectroscopy (0.3 atoms/nm²).¹⁷ The sample preparation for transmission electron microscopy and spectroscopy involved conventional sawing, polishing, grinding, and finally ion milling at rather low energy of 2.5 keV, which resulted in highly radiation-damage resistant TEM samples.¹⁷ Electron energy-loss spectra (EELS) were recorded in a dedicated scanning transmission electron microscope (STEM, VG HB501UX) run at 100 kV and equipped with a parallel EELS spectrometer and an EDX detector. The measurements of spatially resolved energy-loss near-edge structures (ELNES) of the oxygen K edge were performed in a spot modus, with energy dispersion of 0.1 eV per channel and effective electron spot diameter between 1 and 2 nm. The energy resolution of the system was 0.8 eV. Extensive experimental TEM investigations of diffusion-bonded twin bicrystals of $\alpha\text{-Al}_2\text{O}_3$ with various misorientations are reported in Ref. 17.

III. PRESENTATION AND DISCUSSION OF RESULTS

A. Metastable variants of the prismatic twin interface

An initial search for metastable lateral translation states of the prismatic twin bicrystal was done by modeling the two grains as rigid blocks, and exploring the energy difference as a function of the relative rigid shift in the boundary plane ($10\bar{1}0$). A complete structural minimization was then performed only for the resulting equilibrium bicrystal configurations. The energetics was calculated via atomistic modeling based on an empirical shell-model potential.⁷ This simple but effective method has hitherto always succeeded in isolating the complete set of possible metastable translation states of the alumina bicrystals,^{2,18,19} which is the only goal of this part of the study.

The lateral translation state $T = T_1\mathbf{e}_1 + T_2\mathbf{e}_2$ is defined in terms of the lattice vectors $\mathbf{e}_1 = [\bar{1}2\bar{1}0]$ and $\mathbf{e}_2 = [0001]$. The reference bicrystal configuration, corresponding to $(T_1, T_2) = (0, 0)$, was constructed from a block of bulk alumina by rotating one half of the crystal by 180° around $[10\bar{1}0]$ with respect to the other half. Since the rotation axis contains an inversion point of the crystal, the rotation generates a mirror-symmetric twin boundary, denoted by M hereafter. Fig. 2 shows the projection of one grain on the prismatic ($10\bar{1}0$) plane: the solid lines correspond to the lattice vectors \mathbf{e}_1 and \mathbf{e}_2 identifying the cell-edges of the orthorhombic supercell used in the calculations. The label M marks the position of the other grain in the reference M configuration, where the interfacial atoms of the two grains face each other at very close distance.

The energetics of the bicrystal as a function of the translation state (T_1, T_2) is shown in Fig. 3. Note how the highest energies correspond to the energy profile for $T_1 = 0$ (showing only two saddle points), while the lowest energies correspond to the energy profile for $T_1 = 1/2$. This can be easily understood by noting that the translation states with $T_1 = 1/2$ reconstruct a highly ordered bulk-like atomic environment with hexagonal symmetry in the $[0001]$ projection. Only two metastable boundary variants are identified, with translation states $(T_1, T_2) = (1/2, 0)$ and $(T_1, T_2) = (1/2, 1/3)$, denoted by G and S, respectively. In the most stable S variant, the two grains are related by a screw-rotation symmetry operation around $\mathbf{e}_3 = [10\bar{1}0]$, while a glide-mirror symmetry operation with respect to ($10\bar{1}0$) relates the two grains in the metastable G boundary configuration.

B. Energetics and atom arrangements

The internal degrees of freedom of the two supercells describing the S and G boundaries were fully relaxed with respect to the LDFT atomic forces. The resulting interface structures are highly ordered and are shown in Fig. 4 and Fig. 5. The interface energy was calculated as the difference between the total energy of the relaxed supercell, and the total energy of an equal number of Al_2O_3 bulk formula-units, divided by the total interface area in the supercell (121.6 \AA^2).

The S boundary variant is the most stable structure of the prismatic twins, with an interface energy of 0.30 J/m^2 , which is the lowest interface energy of the alumina boundaries studied so far from first-principles (0.63 J/m^2 for the $\Sigma 7$ rhombohedral,² 0.73 J/m^2 for the $\Sigma 3$ basal,¹⁸ and 1.88 for the $\Sigma 13$ pyramidal¹⁹ twins). The metastable G variant is characterized by a higher interface energy, 0.49 J/m^2 , but still very low if compared to the basal and rhombohedral twins. These values correspond to zero excess volume (no expansion along T_3),

therefore it is expected that a cell-volume minimization would further reduce the calculated interface energies. However, the energy lowering due to the inter-granular separation is always very small (of the order of some mJ/m^2), particularly the one for highly ordered boundary structures. As a consequence, this is a case in which the relaxation with respect to the inter-granular separation will certainly be very small and can therefore safely be neglected.

For completeness, the S and G boundary variants were also structurally relaxed according to the shell-model forces. The resulting structures were similar to the corresponding LDFT ones. The shell-model calculations predict the correct energy ordering between the S and G interfaces, with absolute values of 0.1 and 0.4 J/m^2 , respectively. It is worth noting that this is not a general rule, since the shell-model predicts the correct qualitative energy ordering between the variants of the rhombohedral $\Sigma 7$ (Ref. 2) and of the $\Sigma 13$ (Ref. 19) twins, but fails in the case of the basal $\Sigma 3$ twin (Ref. 18).

1. The screw-rotation twin S

The structure of the prismatic screw-rotation twin interface relaxed via LDFT is shown in Fig. 4. The interface, marked by dashed lines, is decorated by Al and O atoms. It is highly ordered, so much that the projection of the twin on the (0001) plane (upper panel) is indistinguishable from the one of the corundum single crystal (upper panel of Fig. 1). If the small interfacial relaxation of the oxygen sublattice is neglected, the boundary does not affect the symmetry of the anion sublattice, that is hexagonal close-packed throughout the supercell. In fact, the twin interface arises mainly from a modified packing of the sublattice of cations, which fills two thirds of the octahedral interstitial sites in the anion sublattice, leaving one third of the sites empty (denoted as “voids” in the following). The arrangement of the voids across the twin boundary can be clearly identified by the symmetric V-shaped pattern.

The Al-O bond lengths of the interfacial atoms are included in Table I, together with the Al-O distances in bulk $\alpha\text{-Al}_2\text{O}_3$ (short $b_s=1.84$ Å and long $b_l=1.96$ Å bonds). The interfacial Al1 and Al2 atoms are six-fold coordinated, with three bond lengths centered around b_s and three around b_l , hence the cation sites are very bulk-like. Since the boundary affects mainly the packing of the cation sublattice in the boundary region, the main changes in coordination number and local atomic environment are shown by the interfacial oxygen atoms. These are distributed between an equal number of three-fold under-coordinated (O3), four-fold coordinated (O4), and five-fold over-coordinated (O5) atomic sites. The O4 anions are bulk-like tetrahedrally coordinated, with two short bonds centered at b_s and two long bonds centered at b_l . The under-coordinated O3 oxygens have three short bonds in a planar geometry, while the O5 anions have one short and four long bonds.

The atoms in the first atomic layer away from the interface are already bulk-like, with Al-O distances of 1.84 and 1.96 Å, therefore showing that the perturbation in the corundum crystal symmetry due to the presence of the boundary is extremely confined to the interface plane, with a transverse extension of less than 2.5 Å (compared for instance to 5-6 Å in the $\Sigma 13(10\bar{1}4)$ twin¹⁹).

2. The glide-mirror twin *G*

The structure of the prismatic glide-mirror twin relaxed via LDFT is shown in Fig. 5. The dashed line marks the position of the interface, that bisects two planes of atoms in this case. The boundary structure has many similarities with that one of the *S* boundary: the (0001) projection is bulk-like and the interface is determined by the cation sublattice only. As a result, the boundary cations are six-fold bulk-like coordinated, while the main changes in the local environment are shown by the boundary anions. Similarly to the *S* variant, these are distributed between three-fold under-coordinated (O3), four-fold bulk-like coordinated (O4), and five-fold over-coordinated (O5) sites (Table I). O3 has three short bond lengths, O4 has two short and two long ones, and O5 has one short and four long ones. The inner atoms neighboring the boundary layer are in a bulk-like environment, therefore the transverse extension of the boundary is again very small in this case ($\leq 4 \text{ \AA}$).

The main distinctions between the two twin models can be summarized by these two points: (1) The stacking sequence of the inequivalent boundary anions along the [0001] (O3-O4-O5 in the *S* boundary, O5-O4-O3 in the *G* boundary), which is accessible by ELNES measurements with spatial single-atom-column resolution. (2) The pattern formed by the cation-void sites across the boundary (V-shaped with one single void at the *S* boundary, V-shaped with a pair of voids at the *G* boundary), which is accessible by quantitative HRTEM analysis.

3. The free prismatic surface

The free prismatic surface was relaxed by means of LDFT in a 60-atom supercell containing six layers of bulk alumina. The transverse size of the supercell was chosen to be big enough so that to minimize the spurious interaction between the free surfaces. These were separated by 9.5 \AA of vacuum and by 6.8 \AA of bulk corundum.

The relaxation involves mainly the two outermost atomic layers, with minor atomic displacements ($\leq 0.05 \text{ \AA}$) in the inner third layer. The main features of the relaxed surface are the outward expansion (0.2 \AA) of the external anions, the inward contraction (0.3 \AA) of the external cations, and the large lateral displacement (0.4 \AA) of the surface anions. The calculated LDFT value for the surface energy is 2.58 J/m^2 .

C. Projected densities of states and ELNES of oxygen

Experimentally, the boundary structure of the $\Sigma 3$ prismatic twin was studied by EELS, measuring the *K*-edge ELNES of oxygen. When ELNES is analyzed by means of the spatial difference technique,²⁰ it gives an indirect information about the local bonding and coordination through a direct measure of the unoccupied electron states present in the neighborhood of an excited atom. These electron states can be obtained from the calculation of the double differential scattering cross section for the excitation of an atom by inelastic electron scattering.²¹ In the special case of the oxygen $1s \rightarrow 2p$ excitations, and in the dipole approximation for the electron scattering, the scattering cross section, and therefore the ELNES *K*-edge for an oxygen site, can directly be related to the calculated site- and *p*-projected density of

states (p -PDOS, p denotes the angular momentum $l=1$).^{22,23} Final-state (core-hole) effects are included in these calculations via the $Z+1$ approximation, where the excited oxygen atom is simulated by a substitutional fluorine impurity atom.^{24,25} The p -PDOS at different excited oxygen sites are calculated from the LDFT one-electron eigenvalues on the $2\times 1\times 1$ \mathbf{k} -point mesh, and smoothed by a Gaussian of 0.8 eV to mimic instrumental and life-time broadening effects.

To see whether the calculated lowest-energy boundary structure is the same as the experimentally observed one, we compare the calculated p -PDOS of the S and G interfaces with the measured ELNES K -edge in Fig. 6. The experimental interface spectrum shows a pronounced peak at 541 eV with a shoulder at higher energies, and a minor peak around 560 eV. The calculated p -PDOS curves for the S and G interfaces are shifted along the energy axis to match the first peaks above the edge onset with the peak at 541 eV in the experimental spectrum. The calculated p -PDOS are very similar to the experimental ELNES, with a good agreement between the relative position and relative height of the peaks. However, they are also very similar to each other, so that, from this comparison, it is not possible with sufficient confidence to discriminate one or the other theoretical boundary structure from the real interface.

The similarity between the p -PDOS can be understood by recalling that they reflect the S and G boundary atomic environments, which are qualitatively and quantitatively very similar (Table I). Fig. 7 shows the breakdown of the total interfacial p -PDOS, displayed in Fig. 6, into the individual contributions corresponding to the O3, O4, and O5 anions. The difference in coordination number affects mainly the low energy region of the spectrum. Over- and under-coordination drives the distinctive “peak and shoulder” shape of the bulk-like atoms, towards a single peaked, and double peaked shape, respectively. These distinctive signals coming from three-, four-, and five-fold coordinated atoms should in principle be measurable by EELS in a STEM with spatial single-atom-column resolution. In this case it would indeed be possible to discriminate between the two boundary structures, even though their p -PDOS are nearly indistinguishable. A line scan along the boundary layers would produce periodic sequences of spectra corresponding to the O3, O4, and O5 anions. The atom-column specific signals for the S and G variants would be similar, but their spatial sequence along the direction $[0001]$ parallel to the interface would be reversed in order, thus allowing to discriminate between the two interfaces: ...-O3-O4-O5-... in the case of the S boundary, ...-O5-O4-O3-... in the case of the G boundary in bicrystals with equivalent bulk orientations. However, for the time being such a level of spatial atom-column resolution is set as a challenge for experimental STEM-EELS microanalysis.³

D. Simulated HRTEM images

For a bicrystal sample of α -Al₂O₃ illuminated by a spatially extended, parallel electron beam along the $[\bar{1}2\bar{1}0]$ zone axis in a high-voltage TEM with atomic-resolution capability, the main feature of the resulting HRTEM image is typically a strong intensity-contrast pattern with intensity extrema at the positions of unoccupied cation sites (cation void sites) in the corundum structure of α -Al₂O₃. The detailed atom-column resolved projection of the bicrystal structure is not directly accessible from the measured HRTEM micrograph. It can be deduced by comparing it via quantitative matching with simulated HRTEM images

from atomistic-model candidate structures.^{26–28} For optimum agreement, all atom-column positions as well as imaging parameters (e.g., defocus, specimen thickness, lens aberrations and transfer function of the recording medium) need to be determined variationally.

As discussed above, we have extracted two metastable structures which should in principle result in different HRTEM images in the $(\bar{1}2\bar{1}0)$ projection. The simulated HRTEM images of the S and G supercells corresponding to a TEM sample thickness of 6 nm and to a defocus value of -20 nm, which are typical parameters for HRTEM of α -Al₂O₃ in an instrument like the JEM ARM-1250 at the MPI für Metallforschung Stuttgart,^{29–31} are displayed in Fig. 8. The two images show characteristic features that allow a discrimination between the two interfaces. In the S variant, the white spots located at the boundary plane are visually equivalent to the ones inside the bulk grains. In the G variant, the interfacial white spots have a distinctively oversized spot, arising from two neighboring spots merging together. The difference in the micrographs does not arise from the interfacial translation states, since both the S and G variants produce a symmetric V-shaped pattern of octahedral void sites, but from the local boundary structure. In particular, the rhombohedral planes of voids in different grains intersect the interface plane precisely at one cation-void site in the S variant (Fig. 4), and on an oxygen basal plane in the G variant (Fig. 5). This is schematically shown by the dashed lines in Fig. 8, where the cation-void sites are associated to the white spots. These images suggest that an high-resolution micrograph would discriminate between the two boundary variants. Experimental HRTEM images^{17,30} show a contrast pattern compatible with the simulated one for the S interface, apparently confirming the LDFT prediction based on the lowest interface energy. Hence, for such experimental images a quantitative HRTEM analysis^{26–28} starting from our calculated two interface models appears promising (cf. Ref. 1).

IV. CONCLUSIONS

In this work, the energetic stabilities, atomistic arrangements and electronic states at the prismatic $\Sigma 3$ ($10\bar{1}0$) twin interface in α -Al₂O₃ were analyzed theoretically by atomistic shell-model and ab-initio LDFT calculations, and experimentally by spatially resolved STEM-EELS measurements of the oxygen *K*-ionization-edge ELNES.

Two metastable microscopic variants for the prismatic twin with low interfacial energies resulted from the theoretical analysis. They exhibit subtle differences in the local arrangements of atoms at their interfaces, which should be distinguishable via TEM bicrystal experiments.

Experimentally, it was demonstrated that a state-of-the-art STEM instrument, with spatial resolution of 1–2 nm and energetical resolution of about 0.8 eV, is not yet capable to resolve the subtle differences in the interfacial ELNES of this very bulk-like twin interface of α -Al₂O₃. However, with the next generation of analytical TEM instruments, which are designed to achieve resolutions of 0.1–0.2 nm in space and about 0.2 eV in energy and currently approaching the stage of operation, the two theoretical twin variants will become distinguishable.

Hence, it is proposed that the present theoretical ab-initio results for the prismatic twin in α -Al₂O₃ provide a very promising benchmark case for the coming analytic TEM instruments: (a) to see whether single-atom-column resolution is really achieved by detecting significant

differences in the oxygen K -edge ELNES for the three distinct interfacial oxygen sites; (b) to check whether the ab-initio LDFT prediction of the S variant with lowest interface energy is also the experimentally observed case. For the ELNES experiment, the spatial sequence of the three oxygen sites is decisive. Alternatively, for a HRTEM experiment combined with a quantitative image-matching analysis, the contrast patterns originating from arrangements of cation-void sites across the interfaces discriminate the two theoretical variants.

ACKNOWLEDGMENTS

This work was supported by the Deutsche Forschungsgemeinschaft (Project No. El 155/4-1). The authors thank Dr. Thomas Gemming for communicating his experimental HRTEM images of a prismatic twin interface prior to publication, Dr. Gunther Richter for his help with the simulation of HRTEM images from the two theoretical twin-interface models, and Prof. Manfred Rühle for his continuous interest and support.

-
- ¹ S. Nufer, A. G. Marinopoulos, T. Gemming, C. Elsässer, W. Kurtz, S. Köstlmeier, and M. Rühle, *Phys. Rev. Lett.* **86**, 5066 (2001).
- ² A. G. Marinopoulos and C. Elsässer, *Acta Mater.* **48**, 4375 (2000).
- ³ K. van Benthem, S. Krämer, and M. Rühle, *Mikrochim. Acta*, (to be published).
- ⁴ B. G. Dick and A. W. Overhauser, *Phys. Rev.* **112**, 90 (1958).
- ⁵ P. Hohenberg and W. Kohn, *Phys. Rev.* **136**, B864 (1964).
- ⁶ W. Kohn and L. J. Sham, *Phys. Rev.* **140**, A1133 (1965).
- ⁷ G. V. Lewis and C. R. A. Catlow, *J. Phys. C* **18**, 1149 (1985).
- ⁸ J. D. Gale, C. R. A. Catlow, and W. C. Mackrodt, *Model. Simul. Mater. Sci. Eng.* **1**, 73 (1992).
- ⁹ M. Wilson, Y. M. Huang, M. Exner, and M. W. Finnis, *Phys. Rev. B* **54**, 15683 (1996).
- ¹⁰ J. D. Gale, *J. Chem. Soc. - Faraday Transact.* **93**, 629 (1997).
- ¹¹ C. Elsässer, N. Takeuchi, K. M. Ho, C. T. Chan, P. Braun, and M. Fähnle, *J. Phys. C* **2**, 4371 (1990).
- ¹² K. M. Ho, C. Elsässer, C. T. Chan, and M. Fähnle, *J. Phys. C* **4**, 5189 (1992).
- ¹³ C. Elsässer, Ph.D. thesis, Universität Stuttgart, 1990.
- ¹⁴ B. Meyer, Ph.D. thesis, Universität Stuttgart, 1998.
- ¹⁵ B. Meyer, C. Elsässer, and M. Fähnle, fortran 90 Program for Mixed-Basis Pseudopotential Calculations for Crystals, Max-Planck-Institut für Metallforschung Stuttgart (unpublished).
- ¹⁶ H. F. Fischmeister, G. Elssner, B. Gibbesch, K. H. Kadow, F. Kawa, D. Korn, and M. Turwitt, *Rev. Mater. Sci. Instrum.* **64**, 234 (1993).
- ¹⁷ S. Nufer, Ph.D. thesis, Universität Stuttgart, 2001.
- ¹⁸ A. G. Marinopoulos, S. Nufer, and C. Elsässer, *Phys. Rev. B* **63**, 165112 (2001).
- ¹⁹ S. Fabris and C. Elsässer, *Phys. Rev. B* **64**, 245117 (2001).
- ²⁰ J. Bruley, *Microsc. Microanal. Microstruct.* **4**, 23 (1993).
- ²¹ M. Nelhiebel, P.-H. Louf, P. Schattschneider, P. Blaha, K. Schwarz, and B. Jouffrey, *Phys. Rev. B* **59**, 12807 (1999).

- ²² R. Brydson, J. Phys. D **29**, 1699 (1996).
²³ S. Köstlmeier and C. Elsässer, Phys. Rev. B **60**, 14025 (1999).
²⁴ C. Elsässer and S. Köstlmeier, Ultramicroscopy **86**, 325 (2001).
²⁵ S. Nufer, T. Gemming, C. Elsässer, S. Köstlmeier, and M. Rühle, Ultramicroscopy **86**, 339 (2001).
²⁶ G. Möbus and M. Rühle, Ultramicroscopy **56**, 54 (1994).
²⁷ G. Möbus, R. Schweinfest, T. Gemming, and T. Wagner, Journal of Microscopy **190**, 109 (1998).
²⁸ P. A. Stadelmann, Ultramicroscopy **21**, 131 (1987).
²⁹ F. Phillipp, R. Höschen, M. Osaki, G. Möbus, and M. Rühle, Ultramicroscopy **56**, 1 (1994).
³⁰ T. Gemming (unpublished).
³¹ G. Richter (unpublished).

TABLE I. Equilibrium Al-O bond lengths (in Å) in the interfacial regions of the S and G supercells. For comparison, the Al-O distances in bulk α -Al₂O₃ are also included. Atoms are numbered as in Figs 4 and 5

Al-O	<i>Bulk</i>						
	1.84	1.84	1.84	1.96	1.96	1.96	
	<i>Screw twin</i>						
Al1-O	1.79	1.86	1.86	1.95	1.95	2.04	
Al2-O	1.83	1.84	1.84	1.90	1.98	1.98	
O3-Al	1.76	1.76	1.79				
O4-Al		1.83	1.83	1.90	2.04		
O5-Al			1.83	2.03	2.04	2.09	2.10
	<i>Glide twin</i>						
Al1-O	1.80	1.81	1.84	1.92	1.94	2.08	
Al2-O	1.76	1.76	1.83	1.91	2.04	2.12	
O3-Al	1.76	1.76	1.76				
O4-Al		1.81	1.84	1.93	1.96		
O5-Al			1.88	1.94	2.05	2.08	2.12

FIG. 1. Corundum structure of $\alpha\text{-Al}_2\text{O}_3$ viewed from the $[\bar{1}2\bar{1}0]$ direction. Light-gray and black circles represent oxygen and aluminium atoms, respectively. The dashed line marks the $(10\bar{1}0)$ plane leading to the prismatic $\Sigma 3$ interface.

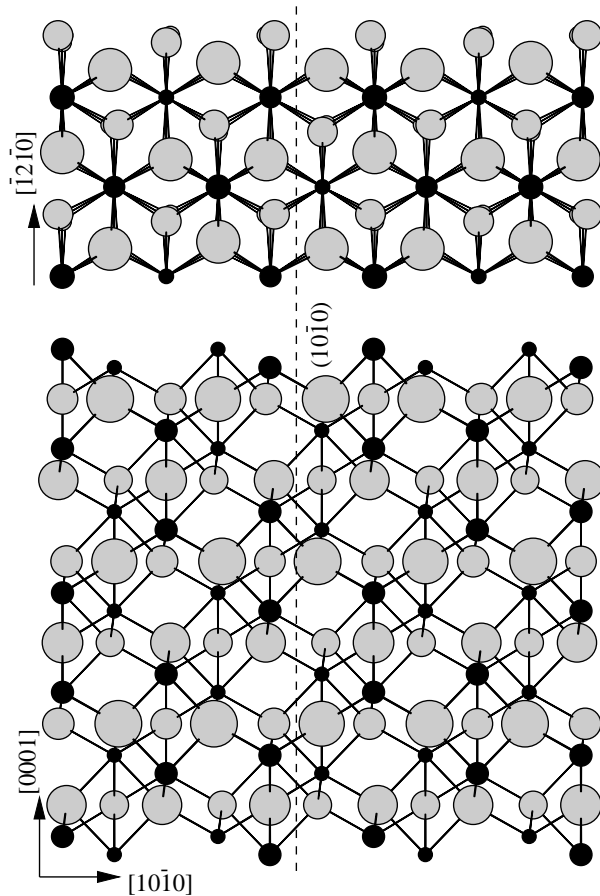


FIG. 2. Atomic structure of one grain projected on the prismatic plane $(10\bar{1}0)$. The in-plane extension of the computational cell is marked by the lattice vectors $\mathbf{e}_1 = [\bar{1}2\bar{1}0]$ and $\mathbf{e}_2 = [0001]$, and by solid lines. M, G and S denote the translation states of the upper grain, leading respectively to Mirror, Glide-mirror and Screw-rotation twins. The atoms are represented as in Fig. 1.

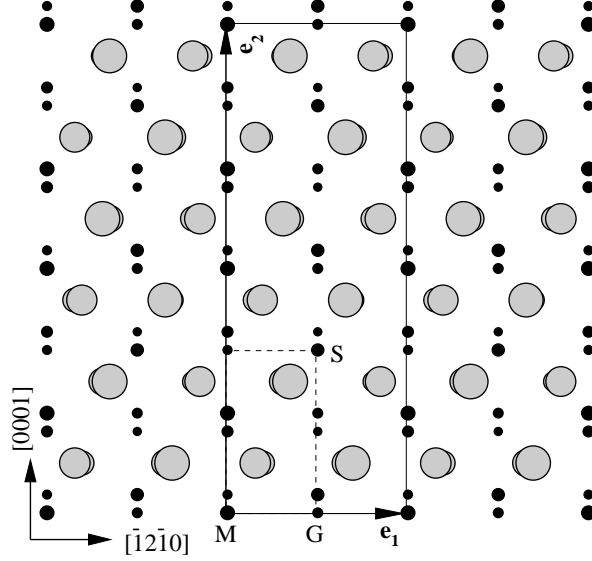


FIG. 3. Shell-model total energy (Ry/supercell) for the twin interfaces as a function of the lateral translation state $T_1\mathbf{e}_1 + T_2\mathbf{e}_2$, with $\mathbf{e}_1 = [\bar{1}2\bar{1}0]$ and $\mathbf{e}_2 = [0001]$.

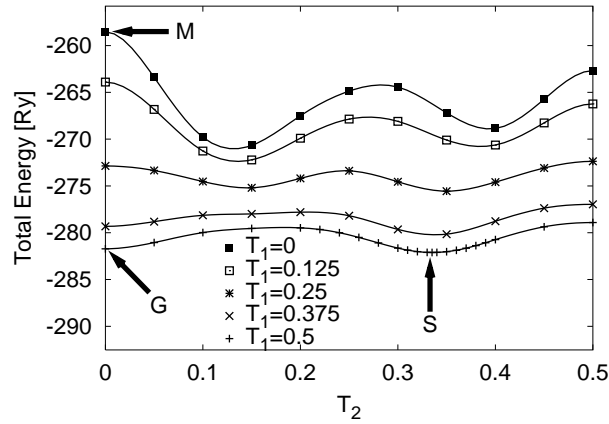


FIG. 4. LDFT result for the relaxed supercell of the S interface viewed along the $[0001]$ (above) and the $[\bar{1}2\bar{1}0]$ (below) directions. The supercell contains two equivalent interfaces (dashed lines), one in the middle, the other at the extremes arising from the periodic boundary conditions in the $[10\bar{1}0]$ direction. The atoms are represented as in Fig. 1.

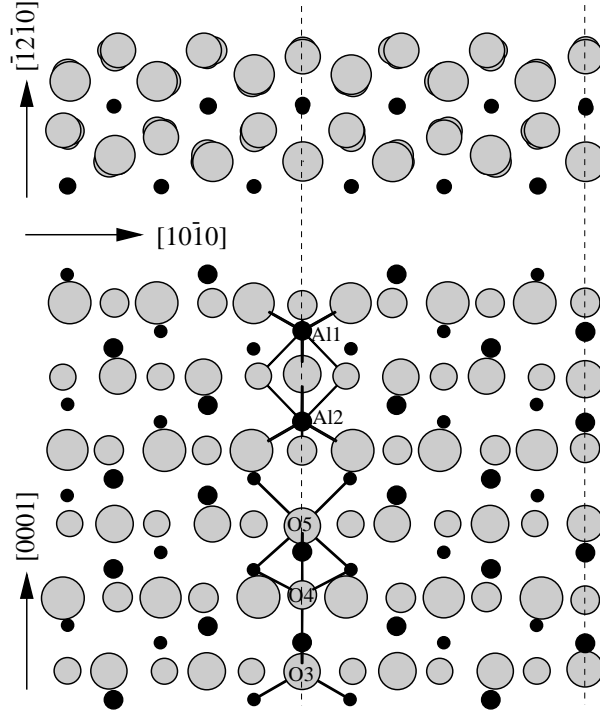


FIG. 5. LDFT result for the relaxed atomic structure of the G interface viewed along $[0001]$ (above) and the $[\bar{1}2\bar{1}0]$ (below) directions. Atoms, labels, and symbols as in Fig. 4.

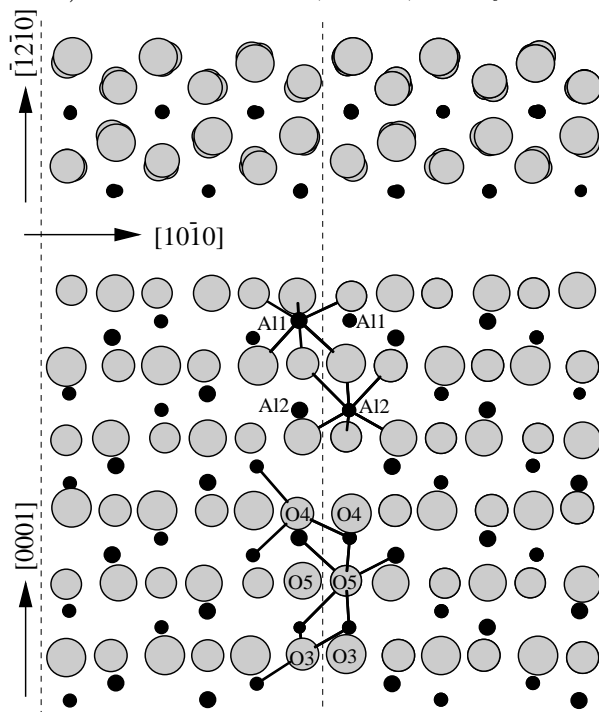


FIG. 6. Comparison between the measured ELNES oxygen K -edge signal and the calculated p -PDOS for the interfacial anions in the G and S boundary variants. (The p -PDOS is the sum of the individual p -PDOS for the three interfacial oxygen sites O3, O4, and O5).

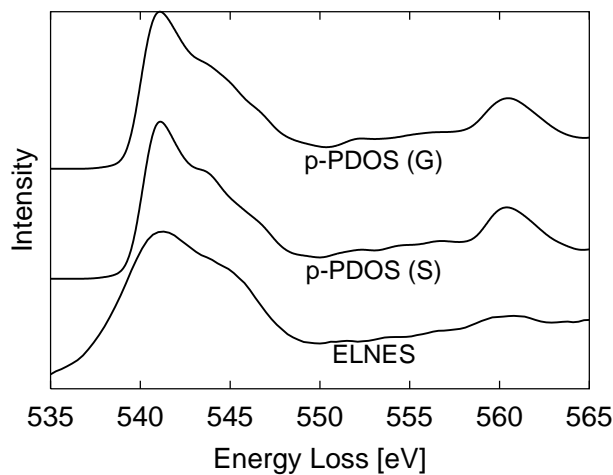


FIG. 7. Individual contributions $D(E)$ of the anions O3, O4, and O5 to the total interfacial oxygen p -PDOS calculated for the S (top) and G (bottom) boundaries.

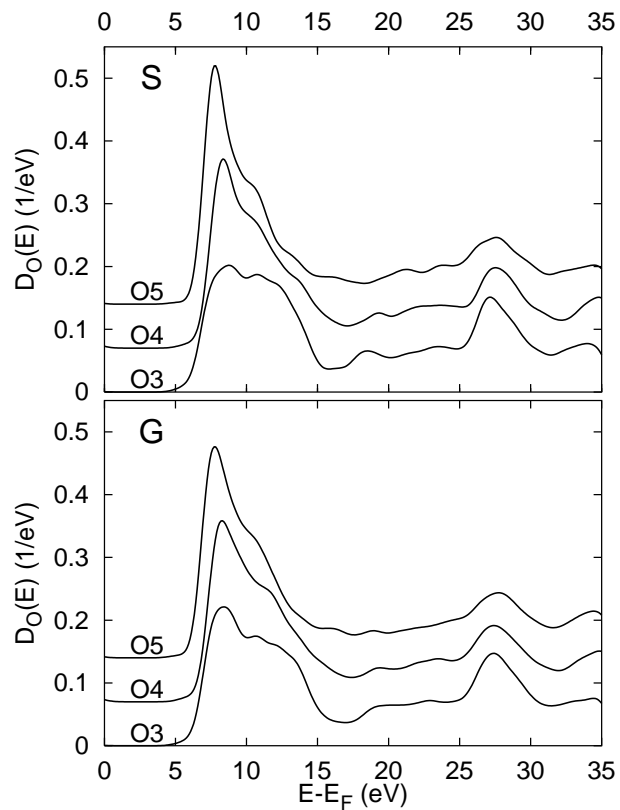


FIG. 8. Simulated HRTEM images of the S and G boundaries. Dashed lines mark the rhombohedral planes.

